Investigating the oxygen evolution reaction on Ir(111) electrode in acidic medium using conventional and dynamic electrochemical impedance spectroscopy

M. Scohy, C. Montella, F. Claudel, S. Abbou, L. Dubau, Frédéric Maillard, E. Sibert, S. Sunde

Investigating The Oxygen Evolution Reaction on Ir(111) Electrode in Acidic Medium Using Conventional and Dynamic Electrochemical Impedance Spectroscopy

M. Scohy,[1,*] C. Montella,[1] F. Claudel,[1] S. Abbou,[1] L. Dubau,[1,*] F. Maillard,[1] E. Sibert,[1] S. Sunde[2]

1. Univ. Grenoble Alpes, CNRS, Grenoble-INP ⊥, Université Savoie-Mont-Blanc, LEPMI, 38000 Grenoble, France

   ⊥ Institute of Engineering Univ. Grenoble Alpes

2. Department of Material Science and Engineering, Norway University of Science and Technology NTNU, 7491 Trondheim, Norway

⊥ Institute of Engineering Univ. Grenoble Alpes

* Corresponding authors: marion.scohy@grenoble-inp.org, laetitia.dubau@lepmi.grenoble-inp.fr

Abstract

In this study, conventional and dynamic electrochemical impedance spectroscopy measurements (EIS and DEIS, respectively) were performed on Ir(111) single crystal electrode and Ir nanoparticles supported onto high-surface area carbon in acidic electrolyte and different potential ranges. We found that the EIS and DEIS results compare fairly well below the onset of oxygen evolution reaction (OER). However, in the OER potential region, some differences were observed between the information derived from these measurements. Cyclic voltammetry and inductively-coupled plasma mass spectrometry experiments revealed that the long time required by EIS cause chemical and structural changes of the Ir(111) surface and oxygen evolution, thus adversely affecting the reliability of the impedance measurement. On the contrary, the short time required for DEIS measurements help mitigating these negative effects, thus highlighting the benefits of such technique to investigate the early stages of surface oxide formation on Ir single crystals.

1. Introduction

The need to increase the energy production from renewable sources and their intermittent nature currently boost the development of energy storage systems such as proton exchange membrane water electrolysers (PEMWEs) [1]. These systems are perceived as one of the most promising technology currently available owing to the possibility of fast start-up, to operate with higher efficiency at higher current density and to sustain larger current variations compared to alkaline water electrolysers [2]. However, the sluggish oxygen evolution reaction (OER, anodic

reaction) kinetics and the poor stability of the anodic material still limit their widespread development [3].

According to volcano plots established more than 30 years ago [4–7], iridium and ruthenium oxides (IrO_2 and RuO_2, respectively) are the most active electrocatalysts for the OER, but only IrO_2 can maintain high electrocatalytic activity on the long term due to the instability of RuO_2 under the harsh operating conditions of a PEMWE anode (acidic pH, highly oxidizing electrochemical potential and atmosphere) reaction conditions [8] [9]. Considering the low abundance of iridium (Ir) on the Earth's crust and its high cost [10], designing and synthesizing tailored OER nanocatalysts is required to minimize the economic and geological constraints associated with its use. Nevertheless, before switching to nanometer-sized catalysts, it is of pivotal importance to understand how Ir surfaces electrochemically oxidize and to establish structure-activity-stability relationships on atomically smooth surfaces such as Ir single crystals [11].

To get answers to the questions, combining cyclic voltammetry (CV) and electrochemical impedance spectroscopy (EIS) techniques appears a promising strategy. However, there is an obvious conflict between the stationary environment required for EIS measurements and the well-known fact that metal surfaces oxidize, buckle, roughen – or even dissolve – under OER conditions, thus questioning the suitability of this technique to the studying of the electrode-electrolyte interface in this potential domain [12]. In the early 1970s Smith *et al*. developed and improved Fourier Transform (FT) methods [13–17]. Later, the introduction and optimization of new algorithms [18–20] combined with Fast FT (FFT) methods led to the development of FFT-EIS [13,21,22], and alternating current (AC) voltammetry [15,16,23,24]. An alternative to frequency response acquisition with FT technique is the application of a stream of wavelets in Hz-kHz frequency range, so-called potentiodynamic EIS or PDEIS [25–27]. More recently, non-stationary electrochemical processes have been studied using this technique [21,28–30]. In

the past few years, multisine signals have been added to this technique, allowing the introduction of dynamic electrochemical impedance spectroscopy (DEIS) [31,32]. In a DEIS measurement, a multisine signal, *i.e*. the sum of sinusoidal signals with different frequencies, is superimposed onto a slow potential ramp and applied to the working electrode. Similar to AC voltammetry, the signal is modulated but, in the latter, only a single sine is applied to the electrode. In DEIS, both amplitudes and phases of the multisine signals are optimized in such a way that the overall amplitude of the potential perturbation is small enough for linearity requirements to be fulfilled, as described by Roy *et al.* [28] and Sacci and Harrington [31]. FFT is subsequently applied to the current recorded during the experiment, in order to separate the responses corresponding to each frequency component in the applied potential and thus monitor the electrochemical impedance for each of these frequencies. The typical time required to acquire a DEIS spectra is less than 1 second, which allows recording electrochemical impedance under dynamic conditions. This technique has been used in corrosion science to study the evolution of pitting processes [33,34] or to investigate the efficiency of corrosion inhibitors [35]. More recently, DEIS has also been employed to unravel the degradation mechanisms of proton-exchange membrane fuel cell (PEMFC) electrodes [36]. In particular, DEIS proved efficient to monitor agglomeration of platinum nanoparticles and crystallite growth.

Herein, we used a similar approach to get insights into the early stages of surface oxidation and the OER mechanism on Ir(111) single crystal electrode and electrochemically activated Ir(111). Impedance measurements were also performed on OER catalysts that are closer to real-life application, such as Ir nanoparticles supported on carbon. Similarities and differences between the EIS and DEIS results are rationalized using cyclic voltammetry and inductively-coupled plasma mass spectrometry experiments.

2. Experimental

Single crystal electrode preparation

An Ir(111) single crystal provided by MaTecK (purity 99.999%, oriented to <0.1°, cylinder with a diameter of 5 mm and a height of 4 mm) was used in this study. Before each experiment, the Ir(111) surface was prepared by annealing in an oxygen-hydrogen flame at 2000°C, cooled in an argon + 5% hydrogen (Ar + 5 % H_2) mixture and protected by a water droplet saturated with this gas mixture. The electrode was then transferred to the electrochemical cell and put in contact with the solution under potential control, at E = +0.8 V *vs*. the reversible hydrogen electrode (RHE). All potentials are referred to the RHE.

Synthesis of Ir/C nanoparticles

A colloidal suspension of Ir nanoparticles was synthesized using dihydrogen hexachloroiridate (IV) hydrate (H_2Cl_6Ir, xH_2O, 99 at. %, Alfa Aesar) and ethylene glycol (EG, Rotipuran ≥ 99.9%, Roth). A 6.95 g_{Ir} L^{-1} solution was first prepared by dissolving H_2Cl_6Ir, xH_2O in Milli-Q grade water (Millipore, 18.2 MΩ cm, total organic compounds <3 ppb). Then, 2.876 ml of this solution were added to 40 ml of EG and 20 ml deionized water under magnetic stirring. The pH was adjusted to 12 by dropwise addition of a 0.5 M NaOH (Suprapur 99.99%, Merck) solution diluted in 1:1 H_2O:EG. The mixture was then heated under reflux and Ar atmosphere at 160°C for 3 hours under constant magnetic stirring, and then allowed to cool down at room temperature under air atmosphere and constant stirring. The second step of the synthesis consisted of adding a high-surface area carbon support to the colloidal suspension. 80 mg of Vulcan XC72 (Cabot) was dispersed in 40 ml of 1:1 H_2O:EG solution and added to the colloidal suspension to obtain a nominal mass fraction of 20 wt.% Ir. The pH was then set to 3 by addition of a 0.5 M H_2SO_4 (Suprapur 96%, Merck) solution diluted in 1:1 H_2O:EG. The solution was stirred for 20 hours before being filtered, washed several times with deionized

water and dried in air at 110°C. Catalytic suspensions were made by mixing 1.8 ml of MQ-grade water, 5.0 mg of catalyst powder, 723 µl of iPrOH and 27 µl of a 5.0 wt % Nafion solution (Electrochem. Inc.). The inks were first sonicated in an ultrasonic bath for 10 min. A 10 µl droplet of ink was deposited on the surface of the glassy carbon electrode (diameter 5 mm) under an N_2 flux until complete evaporation of the solvents, leading to a targeted Ir loading of 20 $\mu g_{Ir}\, cm_{geo}^{-2}$.

Electrochemical measurements

Electrochemical experiments were carried out at room temperature in a cell made of Pyrex glass. All glassware used in this study was initially cleaned with Caro's acid (98% H_2SO_4 mixed with 30% H_2O_2) and carefully rinsed with Milli-Q grade water (Millipore, 18.2 MΩ cm, total organic compounds <3 ppb). The working electrode was either Ir(111) single crystal or a glassy-carbon tip coated with Ir nanoparticles (NPs) supported onto Vulcan XC 72 in fixed mode. The single crystal was used in the hanging meniscus configuration, following the protocols described in Refs. [37–39]. A platinum grid was used as the counter electrode. The reference electrode was a freshly–prepared reversible hydrogen electrode (RHE) connected to the main cell compartment by a Luggin capillary. All the potentials mentioned in this study are referred to that of the RHE.

The electrolyte was a freshly prepared 0.05 M H_2SO_4 solution obtained by diluting Suprapur 96 wt. % H_2SO_4 (Merck) with Milli-Q water. The solution was degassed with Ar (Ar >99.999 %, Messer) before each experiment. Cyclic voltammetry and EIS measurements were realized using an Autolab PGSTAT302N potentiostat. The DEIS measurements were performed using the experimental setup presented elsewhere [36]. The ratio of the potential sweep rate (v_b) on the minimum frequency (f_{min}) was v_b/f_{min} = 2 mV (typically $Fv_b/RT << 2\pi f_{min}$ [31] where F, R and T have their usual meaning) to minimize the parasitic effect of potential ramp on the *ac*

response at low frequency. We used the baseline correction implemented by Sacci *et al*. in Ref. [32].

Before any EIS or DEIS measurement, five cyclic voltammograms (CVs) between 0.05 V and 0.95 V at a sweep rate of 50 mV s^{-1} were performed to control the cleanliness of the Ir(111) single crystal surface. Between the control CVs and the EIS/DEIS measurements, the electrode potential was maintained at 0.8 V. The EIS and DEIS measurements directly followed the control CVs. EIS and DEIS measurements were also performed on an 'electrochemically-activated' Ir(111) surface formed by cycling 15 times the potential between 0.05 to 1.60 V at 50 mV s^{-1}. The same EIS and DEIS procedures were applied to Ir NPs supported on Vulcan XC72 after an activation step composed of 100 CVs between 0.05 and 1.40 V at 500 mV s^{-1} (leading to a stable electrochemical signature of the surface [40]).

The EIS measurements were performed from 0.05 V to 0.95 V at intervals of 20 mV in the frequency range from 10 kHz to 10 mHz applying AC amplitude of 10 mV_{RMS}. (V_{RMS} is the square root of the mean square of the values for one period of the sinusoid). The frequency range of the DEIS measurements was imposed by the sweep rate. It was ranging from 10 kHz to 5 Hz and from 10 kHz to 2.5 Hz for CVs performed at 10 mV s^{-1} or 5 mVs^{-1}, respectively. A homemade Matlab program based on the Levenberg-Marquardt algorithm [41] was used to fit the EIS and DEIS data.

Inductively-coupled plasma mass spectrometry (ICP-MS) and X-ray photoelectron spectroscopy (XPS) measurements

Aliquots of the electrolyte after EIS and DEIS measurements were analyzed using a PerkinElmer NexION 2000 ICP-MS (PerkinElmer, Inc., Waltham, Massachussetts, USA). A 5 µg L^{-1} solution of ^{115}In was used as internal standard for detection of ^{193}Ir. 5 standard solutions were prepared with the following concentrations of Ir: 0.01, 0.05, 0.1, 0.2, 0.5 µg L^{-1}.

XPS analyses were also performed on as-prepared and electrochemically-activated Ir(111) electrode using a Thermo Scientific K-alpha spectrometer with a monochromatized Al X-ray source ($h\nu$ = 1486.6 eV; spot size = 400 µm). Pass energies of 30 and 100 eV were used to record the core level and the survey spectra, respectively. All spectra were acquired using an electron flood gun to compensate possible positive charge accumulation during measurements. The obtained spectra were fitted using Thermo Scientific™ Advantage Software.

3. Results and discussion

EIS and DEIS measurements were performed in two different potential regions: from 0.05 V to 0.95 V or from 0.05 V to 1.45 V on as-prepared (fresh) Ir(111) and on 'electrochemically-activated' Ir(111) single crystal electrodes, respectively. In the first potential region, only adsorption reactions occur, [42] thus establishing the relevance of the DEIS measurements. In the potential region ranging from 1.45 V to 1.60 V, oxygen evolution rendered EIS measurements challenging due to the formation of gas bubbles, and chemical, morphological and structural changes of the electrode surface [43,44]. We will show that DEIS measurements do not suffer from these limitations.

3.1.Potentials below oxygen evolution

3.1.1. As-prepared Ir(111) single crystal electrode (0.05 < E < 0.95 V)

We first compare the results of the EIS and DEIS measurements in the potential region 0.05 < E < 0.95 V. After the preparation of the Ir(111) single crystal, CVs between 0.05 V and 0.95 V at a sweep rate of 50 mV s^{-1} were performed to control the cleanliness of the surface. The features displayed in **Figure 1a** are similar to those reported in previous works [38,45–47]. The peaks related to adsorption/desorption of under-potentially-deposited hydrogen are observed at 0.075/0.095 V, respectively. The double layer region ranges from 0.2 to 0.95 V. Given the

strong surface sensitivity of CVs to the surface state of the electrode, no change of the CV features during potential cycling indicates that the electrode surface is stable in this potential domain. Following these control CVs, EIS and DEIS measurements were performed at 0.05, 0.25, 0.45, 0.65, 0.85 and 0.95 V and from 0.05 to 0.95 V at 10 mV s^{-1}, respectively. The data obtained are represented in **Figure 1b** and **Figure 1c** and in **Figure 1d** and **Figure 1e** in the Nyquist plot and in the Bode modulus representations, respectively.

Figure 1

As evidenced by **Figure 1**, similar impedance spectra were obtained using EIS and DEIS: these are composed of vertical lines in Nyquist representation. In the Bode representation, two asymptotes, one nearly equal to 0 at high frequencies and the second a straight line with a negative slope at low frequencies, associated to a capacitive behavior, are shown. The agreement between the DEIS and EIS suggest that the DEIS technique reliably monitors impedance spectra on Ir(111) single crystal electrode.

In the potential region $0.05 < E < 0.95$ V, only adsorption (*e.g.* sulfate anions) [Eq. (1)] or electrosorption (*e.g.* H-UPD) [Eq. (2)] reactions take place:

$$A + s \leftrightarrow A,s \quad (1)$$

$$H^+ + s + e^- \leftrightarrow H,s \quad (2)$$

where s is an adsorption site and A,s or H,s are adsorbed species.

In the case of an ideally polarizable interface (*i.e.* the electrode is not subject to Faradaic reaction), the electrode impedance results from the series association of the double-layer capacitance and the electrolyte resistance. On the other hand, the impedance for electrosorption reactions can be modeled by a capacitance (C_{ads}) in series with a charge transfer resistance (R_{ct})

representing the kinetic of the adsorption. The double-layer charging is associated with a single capacitance (C_{dl}) in parallel to the adsorption. Finally, a resistance (R_{el}) is added in series for the electrolyte Ohmic drop. The expression of the impedance (Z) is then [48]:

$$Z(p) = R_{el} + \frac{1}{pC_{dl} + \frac{1}{Z_f(p)}} \quad (3)$$

with Z_f the Faradaic impedance and p Laplace variable

$$Z_f(p) = R_{ct} + 1/pC_{ads} \quad (4)$$

Indeed, if the kinetics of electrosorption is too fast versus the probing tool, it cannot be estimated and the associated transfer resistance become negligible [49]. In that case, the **Equation 3** simplifies as:

$$Z(p) = R_{el} + 1/pC_t \quad (5)$$

where $C_t = C_{ads} + C_{dl}$

Since only one time constant is observable in the Bode plots (**Figure 1d** and **Figure 1e**), this indicates that the charge transfer resistance of electrosorption cannot be estimated in the present experimental conditions. Therefore, we will later only use **Equation 5** to fit data at each EIS measurement's potential. For DEIS experiments, although the potential is continuously scanned, the scan rate is low enough, compared to minimum frequency (see experimental [31]) to consider that the system is at steady state and the fit procedure is used.

As shown by **Figure 1b** and **Figure 1c**, due to the small deviation from a perfect vertical line, it was not possible to fit properly the measured data with **Equation** 5. A non-ideal capacitance, also called Constant Phase Element (CPE) ($Z_{CPE} = 1/Q(j\omega)^{\alpha}$ where $j = (-1)^{1/2}$ here, Q is the CPE capacitance parameter and α the CPE exponent) was thus used instead of the ideal capacitance predicted by the theory. Several explanations have been suggested to justify this non-ideal behavior, such as the presence of traces of chemical impurities in the solution [50] or local

variations of the impedance resulting from the hanging meniscus configuration used in the electrochemical experiments [50,51].

Figure 2

As shown in **Figure 2c**, an excellent agreement was obtained between the theoretical and the experimental results. Note that, for the sake of clarity, the data are presented in the complex capacitance representation, where $C = \frac{1}{j\omega Z}$. By applying this model to the entire series of DEIS measurements, the values of Q and α could be extracted for all the electrode potentials. The obtained CPE exponent values, plotted in **Figure 2b**, are close to 1 except for the under-potentially adsorbed hydrogen desorption region, validating the nearly capacitive behavior. An equivalent capacitance was calculated from the Q formula proposed by Brug *et al*. [52].

$$C_t = Q^{\frac{1}{\alpha}} \left(R_{el}^{-1}\right)^{1-\frac{1}{\alpha}} \quad (6)$$

Figure 2d also outlines the good consistency between the calculated capacitances from the EIS and DEIS spectra (using **Equation 6**) and the capacitances extracted from the typical CV of the as-prepared Ir(111) electrode using **Equation 7**:

$$C_t = \frac{j}{v_b} \quad (7)$$

where v_b is the potential sweep rate.

Hence, in summary, the results presented in this section show that DEIS can be used to determine the impedance of the electrochemical system under consideration.

3.1.2. Electrochemically-activated Ir(111) electrode (0.05 < E < 1.45 V)

The same series of experiments were performed on an 'electrochemically-activated' Ir(111) electrode prepared by sweeping the potential of the as-prepared Ir(111) electrode 15 times at 50 mV s^{-1} between 0.05 to 1.60 V. The electrochemical activation protocol is aimed at forming an oxy-hydroxide layer that is more active than metallic iridium towards the OER [44,53]. It is documented in the literature [54–57] that potential cycling above 1.4 V leads to the growth of an oxide film [54,58]. In this study, sweeping the electrode potential up to 1.6 V resulted in a more active but also more stable surface state relative to Ir(111) in agreement with literature [59]. The Ir4f spectra measured on the fresh and 'electrochemically-activated' Ir(111) surfaces are displayed in **Figure 3**. The XPS spectrum on the fresh Ir(111) surface features on contribution 60.9 eV and another at 63.9 eV associated to metallic iridium [55,60]. These peaks are shifted by *ca.* 0.3 eV (61.2 eV) and a small shoulder emerges at 62 eV thus reflecting the presence of Ir(IV) [60–63] on electrochemically-activated Ir(111) surface (a poorer fit was obtained upon including an Ir(III) component).

Figure 3

Figure 4a displays the CV of the 'electrochemically-activated' Ir(111) electrode. Compared to the CV recorded on the as-prepared Ir(111) (**Figure 1a**), broader hydrogen adsorption/desorption peaks and higher current associated to the pseudo-capacitance of the oxy-

hydroxide layers were observed. Moreover, new redox peaks emerged at *ca*. 0.95 V associated to the transition from Ir(III) to Ir(IV) [62,64–66]. A small peak, more pronounced on the reduction part of the curve and overlapping with the beginning of the OER, at *ca*. 1.45 V developed upon potential cycling. According to literature, this pair of peaks may be ascribed to the oxidation of Ir(IV) to Ir(V/VI) [64,66,67] but a recent study from Pfeifer *et al.* [68] attributes this peak to the oxidation of O(II-) species present in the iridium oxide layer to O(I-) species contained in the adsorbed OH species.

After electrochemical activation, the electrode potential was swept back to 0.05 V and EIS measurements were recorded every 20 mV up to 1.45 V. The preparation protocol was repeated to perform DEIS measurements from 0.05 to 1.45 V at 10 mV s^{-1}. The Nyquist representation of the DEIS data obtained at 0.65 and 1.25 V are shown in **Figure 4b** and **Figure 4c**, respectively. Similar to what was observed on the as-prepared Ir(111) electrode, and in agreement with theoretical expectations, vertical lines associated with a pure capacitive behavior were obtained. Note that, due to the hanging meniscus configuration, the value of the high-frequency resistance was found higher than the predicted electrolyte resistance [69] ($R_{el\ theoretical}$ = 7.25 Ω cm²). Nevertheless, the similar high-frequency resistance determined by EIS and DEIS measurements validate the DEIS protocol. However, the non-negligible gain of time provided by the DEIS opens the way to impedance measurements in non-steady-state conditions.

Figure 4

3.2.Potentials above the oxygen evolution (1.45 V < E < 1.60 V)

The second part of this study focuses on the potential region comprised between 1.45 V to 1.60 V, a potential region in which the Ir(111) surface oxidizes very quickly (similar to what was found for 0.05 V < *E* < 1.45 V). In addition, the Ir(111) surface can dissolve electrochemically and the OER takes place in this potential domian, [43,44] thus rendering EIS measurements highly challenging (no steady-state is achieved). We will show that DEIS is an appropriate technique to obtain information about the electrode | electrolyte interface while avoiding problems linked to these transient phenomena.

3.2.1. As-prepared Ir(111) single crystal electrode

Figure 5c displays the LSV recorded on the as-prepared Ir(111) electrode during potential cycling between 1.45 and 1.60 V. We first remark an increase of the geometrical current density at potentials located above 1.47 V, thus signing the onset of a new Faradaic process. Although this potential is very close to the thermoneutral voltage of the OER, we notice that such increase may also correspond to the O(II-)/O(I-) redox couple [70] or to the dissolution of Ir atoms [71]. Impedance measurements were performed from 1.45 to 1.60 V with a step increase of 5 mV for each EIS measurement and with a potential sweep rate of 5 mV s^{-1} for DEIS measurements. The results are plotted in the Nyquist representation in **Figure 5a, 5b, 5d and 5e**. The appearance of a semi-circle in DEIS and EIS measurements in the potential region 1.45 < *E* < 1.50 V vs. RHE confirms that a charge transfer process (electrosorption-desorption reaction in this case) takes place at the electrode surface. This semi-circle becomes more pronounced at *E* > 1.55 V in agreement with the increase of the current density shown in **Figure 5c**.

Figure 5

In contrast to the former case (0.05 V < E < 1.45 V), significant differences emerge from the comparison of the EIS and DEIS data. Based on the expression of the impedance for an electrosorption-desorption process [48,72], this can be rationalized assuming different surface coverages or concentrations of species at the interface, which result from the large time required for EIS measurements (*ca*. 5 min). **Figure 6a** shows the current–time transients recorded during stepping the potential from 0.8 V to 1.4, 1.5 or 1.6 V, thus simulating the potential variations during EIS measurements. For $E \leq 1.50$ V, a fast rise in current is observed, then the current decays reaching a value close to 0 mA cm^{-2}. In contrast, at $E = 1.60$ V, after a fast decrease (~3 s), a current maximum is observed after which the current stabilizes around 1 mA cm^{-2}. Based on the work of Özer *et al*. [59], the electrode surface is believed to roughen in these potential conditions. This atomic roughening enhances the intrinsic OER activity of Ir(111), and may account partially for the gain in OER current. The progressive oxidation of non-stoichiometric Ir-O species, hydroxy-groups and water molecules of the topmost and near-surface layers formed at the beginning of the OER in the experimental conditions of EIS measurements may also account for the observed catalytic trend [73], as well as the oxidation of oxygen from O(II-) to O(I-) species [68].

Figure 6b compares the CVs recorded on the as-prepared Ir(111) electrode before and after the EIS (dashed black line) or the DEIS (plain red line) measurements (note that the potential was swept negatively after the (D)EIS measurements). We first remark that the underpotentially-adsorbed/desorbed hydrogen features are strongly distorted, and their intensity is depreciated after the EIS measurement, thus confirming buckling and atomic roughening of the electrode surface. Due to the shorter acquisition time (*ca.* 40 s for this potential range), these phenomena are less pronounced after the DEIS measurement. Furthermore, the higher double-layer current observed after the EIS measurement suggests that the growth of the hydrous oxide layer on Ir(111) was much less important during the DEIS measurement. An oxygen reduction reaction

(ORR) current also manifests in the negative-going potential scan recorded after the DEIS or the EIS measurements. Here again, the ORR current is less pronounced after the DEIS measurement, and this is in line with the shorter time required associated with the measurement.

Finally, **Figure 6c** shows that the as prepared Ir(111) surface is much more active toward the OER after the EIS relative to after the DEIS measurement. This agrees with the non-monotonic dependence of the OER activity as a function of time recently reported by Li *et al*. [73] and others [59], and again should be associated with continuous growth of an oxy-hydroxide film on the metal surface. The enhanced OER activity of the Ir(111) electrode after the EIS measurement thus confirms that the electrode surface was in average more oxidized after the EIS measurement than after the DEIS measurement [68,74]. The large differences of the voltammograms recorded in the OER region before and after EIS and DEIS measurements on as-prepared Ir(111) and electrochemically-activated Ir(111), represented in **Figure 6c** and **Figure 6d,** support these hypotheses. In contrast, almost no difference in OER activity can be noticed after EIS and DEIS measurements on the electrochemically-activated Ir(111) electrode because a more stable surface state was previously achieved during the potential cycling protocol (**Figure 6d**).

Figure 6

In summary, thanks to its faster acquisition process, the DEIS technique proved capable to dynamically measure the electrochemical impedance of metallic Ir single crystal with only minimal changes of the electrode structure and chemistry (mild oxidation of the surface). In contrast, the long acquisition time required for EIS measurements leads to important changes

in the structure and the chemistry of the single crystal surface due to the formation of an oxy-hydroxide film and the early stages of the OER.

3.2.2. Electrochemically-activated Ir(111) electrode

To confirm our claims, a fresh Ir(111) electrode was electrochemically-activated using the protocol discussed previously. Impedance measurements were then performed from 1.45 to 1.60 V with a step increase of 5 mV (EIS measurements) and with a potential sweep rate of 5 mV s^{-1} (DEIS measurements). The linear sweep voltammogram mimicking the applied potential variations during DEIS measurements is displayed in **Figure 7c**. Similar to what was observed on the as-prepared Ir(111) electrode, a nearly 2-fold enhancement of the OER activity was monitored on the electrochemically-activated Ir(111) electrode relative to the as-prepared Ir(111) electrode, in agreement with literature [59,75]. **Figure 7a**, **Figure 7b**, **Figure 7d** and **Figure 7e** show that the Nyquist plots are composed of a semi-circle arc with a frequency shift as the electrode potential is increased. Due to the minimum frequency used in this work, f_{min} = 2.5 Hz, only the high-frequency part (bent line) of the semi-circle graph is observed at the lower electrode potentials (**Figure 7a** and **Figure 7d**). We, however, notice a decrease in the impedance values measured on 'electrochemically-activated' Ir(111) electrode compared to as-prepared Ir(111) that is consistent with the higher OER activity of the 'electrochemically-aged' Ir(111) electrode in comparison with as-prepared Ir(111). Unlike what was observed on as-prepared Ir(111) electrode in this potential range, the results of the DEIS and EIS data are nearly similar. **Figure 6d** confirms this similarity by exhibiting identical CVs before and after the EIS measurements. These findings agree with previous reports pointing toward less pronounced changes of the OER activity for electrochemically oxidized Ir electrodes compared to metallic Ir electrodes upon polarization in the OER potential region [43,59].

Figure 7

To get insights into the chemical changes occurring on the Ir electrodes during EIS or DEIS measurements, ICP-MS measurements were performed on electrolytes used for the impedance experiments on as-prepared Ir(111) and 'electrochemically-activated' Ir(111) electrodes. In agreement with all the above, whatever the nature of the electrode, lower Ir concentration was found after DEIS compared to EIS measurements (**Table 1**). Nevertheless, it is noteworthy that higher Ir concentrations were monitored on the 'electrochemically-activated' Ir(111) electrode in comparison to the as-prepared Ir(111) electrode. This trend confirms former literature reports [44] and can be rationalized by considering the presence of unstable Ir-species and lattice defects in the oxy-hydroxide layer as well the higher surface area of the electrochemically-activated Ir(111) electrode [67,76].

Table 1

Combined with the CV results, the ICP-MS measurements thus confirm that lower chemical and structural changes of the single crystal surface were observed during the DEIS measurement, corroborating the interest of DEIS to perform impedance measurements in the OER region.

3.2.3. Ir nanoparticles supported on high surface area carbon

Finally, for the sake of generalizing our findings to real-life OER catalysts, we extended our approach to Ir nanoparticles supported on high surface area carbon (Ir/C) synthetized by a modified polyol method (note that similar results were obtained on Ir nanoparticles supported on antimony-doped tin oxide, not shown). **Figure 8** shows that the EIS (on the left side) and DEIS (on the right side) spectra recorded on Ir/C resemble those obtained on as-prepared

Ir(111) and electrochemically-activated Ir(111) electrode at low frequencies, starting from a bent line to semi-circles. In the high frequency region of both spectra, we however noticed a change of diagram shape attributed to the porosity of both carbon support and Ir NPs. The data at potentials above 1.50 V were fitted using the model of porous electrode proposed by Meyers et al. [77] in the case where the solid conductivity is very large compared to the electrolyte conductivity (**Equation 8**).

$$Z(p) = A\ Z_{loc}(p)^{1/2}\ \coth(B/Z_{loc}(p)^{1/2}) \quad (8)$$

with $A = \frac{1}{S(S_p K_m)^{1/2}}$ and $B = L(S_p/K_m)^{1/2}$

where S is the geometric surface of the electrode, S_p is the electroactive surface of the pores per unit volume, K_m the conductivity of the electrolyte filled with bubbles in the pores, L the thickness of the porous layer and Z_{loc} the local impedance at the pores surface.

The expression of the local impedance Z_{loc} is in this case (**Equation 9**):

$$Z_{loc}(p) = R_{ct}/(1 + (\tau\, p)^{\alpha}) \quad (9)$$

with $\tau = (R_{ct}\, Q_{dl})^{1/\alpha}$

The result of the fit obtained at 1.6 V for EIS data is presented in **Figure 8c**, indicating a good adequacy between the model used and the experimental data. An increase in the high-frequency resistance with potential is apparent in the impedance-plane plots, which we associate with the presence of oxygen bubbles at the interface [78]. This issue was clearly avoided when the DEIS technique was used.

Figure 8

3.3. Comparison of Tafel slopes derived from EIS/DEIS measurements and OER polarization curves

In **Figure 9**, we tentatively fitted the different sets of data obtained in the OER region using the equivalent circuit based on a charge-transfer reaction with double-layer charging and Ohmic potential drop (**Figure 9a**). One example of fit is shown in **Figure 9b**. The EIS/DEIS spectra feature only one semi-circle in the frequency range explored ($f \geq 2.5$ Hz), thus preventing getting insights on the OER mechanism, as well as discriminating between several possible reaction pathways.

Figure 9

The OER polarization curves of as-prepared Ir(111) and electrochemically-activated Ir(111) electrodes are shown in **Figure 9c** (note that the current was corrected from the Ohmic drop *a posteriori*). At low potentials, between 1.50 V and 1.60 V for as-prepared Ir(111) and between 1.48 V and 1.55 V for 'electrochemically-activated' Ir(111) electrodes, the Tafel slope approaches 46 mV dec^{-1}. At higher electrode potential, the Tafel slopes change, pointing toward a possible change of the rate determining step of the OER mechanism.

Figure 9d displays the reciprocal of the charge transfer resistance obtained by fitting the EIS and DEIS spectra as a function of the electrode potential. A linear behavior was observed. The Tafel slopes determined from the OER polarization curves in the low current density region and calculated from the EIS and DEIS spectra are shown in **Table 2**. In general, a good agreement was obtained between the values derived from OER polarization curves and the DEIS measurements, but higher Tafel slopes were obtained from EIS measurements. Based on the calculations described above, the higher Tafel slopes values obtained by EIS may be rationalized by considering that the surface was more strongly oxidized in these experimental

conditions (higher oxygen coverage at the surface during the measurement [48], which can be seen in **Figure 6b** as well).

Whereas stationary impedance spectra featured an increased series resistance due to bubble formation at the Ir nanoparticles, the series resistance in the impedance data collected through DEIS were not affected. This indicates that the DEIS data were in general less affected by gas evolution. The shorter collection time will mitigate any adverse effects on the analysis from the presence of gas at and in the vicinity of the electrode. Tafel slopes calculated from the apparent charge-transfer from the DEIS data increase at high currents in a similar fashion as the Tafel slope from the polarization curve. We thus concluded that the higher Tafel slope at high current density is related to the OER mechanism and not to the formation of oxygen bubbles. Indeed, it is well-established that the OER involves multiple reaction steps. Several OER mechanisms have been proposed in the 1950-1960s by Bockris [79] and Krasil'shchikov [80] They are all based on an electrosorption step followed by other steps which might be a combination, or other electrosorption/desorption steps [81]. The theoretical Tafel slopes for the 'oxide-path' and 'electrochemical-oxide' paths are presented in **Table 2**. The Tafel slopes obtained from OER polarization curves seem to advocate for the electrochemical path, the rate-determining step being the second step at low current densities. In contrast, the Tafel slopes obtained by DEIS were in favor of the oxide path, the rate-determining step being one of the two chemical steps. The *ca*. 20 mV difference between the measured values renders any quantitative interpretation risky, if experimental incertitude and data dispersion are taken into account. These differences in Tafel slopes are also a consequence of different dissolution mechanisms [44,67,75,76], since this experiment cannot deconvolute dissolution of Ir from OER. Furthermore, for both mechanisms, when the first step becomes rate-determining, the Tafel coefficient increases to 119 mV dec^{-1}. This trend is clearly visible at higher current densities on **Figure 9c** and was already reported by others [82].

Table 2

4. Conclusions

In this study, impedance spectra were measured by conventional and dynamic impedance spectroscopy (EIS and DEIS, respectively) on as-prepared Ir(111), 'electrochemically-activated' Ir(111) and Ir nanoparticles supported onto high surface area carbon. The EIS and DEIS results were comparable but DEIS allowed an important gain of time with respect to conventional EIS. DEIS technique also revealed as powerful tool to study dynamic (transient) systems and circumvent some limitations of EIS. We demonstrated this by investigating oxygen evolution reaction (OER) on a freshly prepared Ir(111) electrode. In OER conditions, the Ir surface undergoes structural (formation of surface defects, buckling and roughening of the crystalline surface) and chemical (surface oxidation and Ir dissolution) changes. The presence of oxygen bubbles that form and detach adds another difficulty to EIS measurements. Thanks to DEIS, a more accurate picture of the phenomena occurring at the Ir(111) electrode | electrolyte interface was achieved. While the EIS and DEIS signature were similar for both as-prepared and electrochemically-activated Ir(111) electrodes at low electrode potentials, only DEIS proved capable to capture the evolution of electrochemical impedance of the Ir(111) surface in OER conditions while minimizing the structural and chemical changes occurring at high potentials. Thanks to the shorter collection time of DEIS, any adverse effect of the presence of gas at and in the vicinity of the electrode was mitigated. Nearly similar values for the Tafel slopes were obtained by DEIS and polarization curves, demonstrating that this technique can be accurately used in transient conditions.

Acknowledgments

This work was performed within the framework of the Centre of Excellence of Multifunctional Architectured Materials "CEMAM" n◦ AN-10-LABX-44-01. The French National Research Agency (MOISE project, grant number ANR-17-CE05-0033) and the PHC AURORA 2017 program (n° 38483VD) financially supported this study.

References

[1] M.Z. Jacobson, Review of solutions to global warming, air pollution, and energy security, Energy Environ. Sci. 2 (2009) 148–173. doi:10.1039/b809990c.

[2] M. Carmo, D.L. Fritz, J. Mergel, D. Stolten, A comprehensive review on PEM water electrolysis, Int. J. Hydrogen Energy. 38 (2013) 4901–4934. doi:10.1016/j.ijhydene.2013.01.151.

[3] A.S. Aricò, S. Siracusano, N. Briguglio, V. Baglio, A. Di Blasi, V. Antonucci, Polymer electrolyte membrane water electrolysis: Status of technologies and potential applications in combination with renewable power sources, in: J. Appl. Electrochem., 2013. doi:10.1007/s10800-012-0490-5.

[4] I.C. Man, H.Y. Su, F. Calle-Vallejo, H.A. Hansen, J.I. Martínez, N.G. Inoglu, J. Kitchin, T.F. Jaramillo, J.K. Nørskov, J. Rossmeisl, Universality in oxygen evolution electrocatalysis on oxide surfaces, ChemCatChem. (2011). doi:10.1002/cctc.201000397.

[5] S. Trasatti, Electrocatalysis in the anodic evolution of oxygen and chlorine, Electrochim. Acta. 29 (1984) 1503–1512.

[6] S. Trasatti, Electrocatalysis by oxides—Attempt at a unifying approach., J Electroanal Chem. 111 (1980) 125–131. doi:10.1016/S0022-0728(80)80084-2.

[7] M.H. Miles, M.A. Thomason, Periodic variations of overvoltages for water electrolysis in acid solutions from cyclic voltammetric studies, J. Electrochem. Soc. 123 (1976) 1459. doi:10.1149/1.2132619.

[8] R. Hutchings, K. Müller, R. Kötz, S. Stucki, A structural investigation of stabilized oxygen evolution catalysts, J. Mater. Sci. (1984). doi:10.1007/BF00980762.

[9] E. Antolini, Iridium as catalyst and cocatalyst for oxygen evolution/reduction in acidic polymer electrolyte membrane electrolyzers and fuel cells, ACS Catal. (2014). doi:10.1021/cs4011875.

[10] I. Katsounaros, S. Cherevko, A.R. Zeradjanin, K.J.J. Mayrhofer, Oxygen electrochemistry as a cornerstone for sustainable energy conversion, Angew. Chemie - Int. Ed. (2014). doi:10.1002/anie.201306588.

[11] N. Danilovic, R. Subbaraman, K.C. Chang, S.H. Chang, Y.J. Kang, J. Snyder, A.P. Paulikas, D. Strmcnik, Y.T. Kim, D. Myers, V.R. Stamenkovic, N.M. Markovic, Activity-stability trends for the oxygen evolution reaction on monometallic oxides in acidic environments, J. Phys. Chem. Lett. (2014). doi:10.1021/jz501061n.

[12] A.S. Bandarenka, Exploring the interfaces between metal electrodes and aqueous electrolytes with electrochemical impedance spectroscopy, Analyst. (2013). doi:10.1039/c3an00791j.

[13] S.C. Creason, J.W. Hayes, D.E. Smith, Fourier transform faradaic admittance measurements III. Comparison of measurement efficiency for various test signal waveforms, J. Electroanal. Chem. 47 (1973) 9–46. doi:10.1016/S0022-0728(73)80343-2.

[14] D.E. Smith, The Acquisition of electrochemical response spectra by on-line Fast Fourier Transform: Data processing in electrochemistry, Anal. Chem. 48 (1976) 221A–240. doi:10.1021/ac60366a046.

[15] R.J. Schwall, A.M. Bond, D.E. Smith, On-line Fast Fourier Transform Faradaic admittance measurements: Real-time deconvolution of heterogeneous charge transfer kinetic effects for thermodynamic and analytical measurements, Anal. Chem. 49 (1977)

1805–1812. doi:10.1021/ac50020a042.

[16] A.M. Bond, R.J. O'Halloran, I. Ruzic, D.E. Smith, A.C. Cyclic voltammetry: A digital simulation study of the slow scan limit condition for a reversible electrode process, J. Electroanal. Chem. 90 (1978) 381–388. doi:10.1016/S0022-0728(78)80073-4.

[17] R.J. O'Halloran, J.C. Schaar, D.E. Smith, Rapid drop time on-line Fast Fourier Transform Faradaic admittance measurements, Anal. Chem. 50 (1978) 1073–1079. doi:10.1021/ac50030a018.

[18] G.S. Popkirov, R.N. Schindler, A new impedance spectrometer for the investigation of electrochemical systems, Rev. Sci. Instrum. 63 (1992) 5366–5372. doi:10.1063/1.1143404.

[19] G.S. Popkirov, R.N. Schindler, Optimization of the perturbation signal for electrochemical impedance spectroscopy in the time domain, Rev. Sci. Instrum. (1993). doi:10.1063/1.1144316.

[20] K. Darowicki, Theoretical description of the measuring method of instantaneous impedance spectra, J. Electroanal. Chem. 486 (2000) 101–105. doi:10.1016/S0022-0728(00)00110-8.

[21] J. Hazi, D.M. Elton, W.A. Czerwinski ' ', J. Schiewe, V.A. Vicente-Beckett, A.M. Bond, Microcomputer-based instrumentation for multi-frequency Fourier transform alternating current (admittance and impedance) voltammetry, J. Electroat~ulytical Chem. 437 (1997).

[22] M.J. Walters, J.E. Garland, C.M. Pettit, D.S. Zimmerman, D.R. Marr, D. Roy, Weak adsorption of anions on gold: Measurement of partial charge transfer using Fast Fourier Transform electrochemical impedance spectroscopy, J. Electroanal. Chem. 499 (2001)

48–60. doi:10.1016/S0022-0728(00)00468-X.

[23] M.E. Van Der Geest, N.J. Dangerfield, D.A. Harrington, An ac voltammetry study of Pt oxide growth, J. Electroanal. Chem. 420 (1997) 89–100.

[24] D.A. Harrington, Ac voltammetry for measurement of surface kinetics, J. Electroanal. Chem. (1993). doi:10.1016/0022-0728(93)80352-I.

[25] G.A. Ragoisha, A.S. Bondarenko, Potentiodynamic electrochemical impedance spectroscopy, Electrochim. Acta. 50 (2005) 1553–1563. doi:10.1016/j.electacta.2004.10.055.

[26] G.A. Ragoisha, A.S. Bondarenko, Potentiodynamic electrochemical impedance spectroscopy of silver on platinum in underpotential and overpotential deposition, Surf. Sci. 566–568 (2004) 315–320. doi:10.1016/j.susc.2004.05.061.

[27] G.A. Ragoisha, A.S. Bondarenko, Potentiodynamic electrochemical impedance spectroscopy. Copper underpotential deposition on gold, Electrochem. Commun. 5 (2003) 392–395. doi:10.1016/S1388-2481(03)00075-4.

[28] J.E. Garland, C.M. Pettit, D. Roy, Analysis of experimental constraints and variables for time resolved detection of Fourier transform electrochemical impedance spectra, Electrochim. Acta. 49 (2004) 2623–2635. doi:10.1016/j.electacta.2003.12.051.

[29] G.A. Ragoisha, N.P. Osipovich, A.S. Bondarenko, J. Zhang, S. Kocha, A. Iiyama, Characterisation of the electrochemical redox behaviour of Pt electrodes by potentiodynamic electrochemical impedance spectroscopy, J. Solid State Electrochem. 14 (2010) 531–542. doi:10.1007/s10008-008-0663-7.

[30] C.M. Pettit, P.C. Goonetilleke, D. Roy, Measurement of diffrential capacitance for

faradaic systems under potentiodaynamic conditions: considerations of Fourier transform and phase-selective techniques, J. Electroanal. Chem. 589 (2006) 219–231. doi:10.1016/j.jelechem.2006.02.012.

[31] R.L. Sacci, D.A. Harrington, Dynamic electrochemical impedance spectroscopy, Electrochem. Soc. 19 (2009) 31–42. doi:10.1149/1.3247564.

[32] R.L. Sacci, F. Seland, D.A. Harrington, Dynamic electrochemical impedance spectroscopy, for electrocatalytic reactions, Electrochim. Acta. 131 (2014) 13–19. doi:10.1016/j.electacta.2014.02.120.

[33] K. Darowicki, S. Krakowiak, P. Ślepski, Evaluation of pitting corrosion by means of dynamic electrochemical impedance spectroscopy, in: Electrochim. Acta, 2004: pp. 2909–2918. doi:10.1016/j.electacta.2004.01.070.

[34] S. Krakowiak, K. Darowicki, P. Slepski, Impedance investigation of passive 304 stainless steel in the pit pre-initiation state, Electrochim. Acta. 50 (2005) 2699–2704. doi:10.1016/j.electacta.2004.11.015.

[35] H. Gerengi, K. Darowicki, G. Bereket, P. Slepski, Evaluation of corrosion inhibition of brass-118 in artificial seawater by benzotriazole using Dynamic EIS, Corros. Sci. 51 (2009) 2573–2579. doi:10.1016/j.corsci.2009.06.040.

[36] M. Darab, P.K. Dahlstrøm, M.S. Thomassen, F. Seland, S. Sunde, Dynamic electrochemical impedance spectroscopy of Pt/C-based membrane-electrode assemblies subjected to cycling protocols, J. Power Sources. (2013). doi:10.1016/j.jpowsour.2013.05.105.

[37] J. Clavilier, R. Faure, G. Guinet, R. Durand, Preparation of monocrystalline Pt microelectrodes and electrochemical study of the plane surfaces cut in the direction of

the {111} and {110} planes, J. Electroanal. Chem. (1979). doi:10.1016/S0022-0728(79)80022-4.

[38] S. Motoo, N. Furuya, Electrochemistry of platinum single crystal surfaces. Part I. Structural change of the Pt (111) surface followed by an electrochemical method, J. Electroanal. Chem. (1984). doi:10.1016/0022-0728(84)80196-5.

[39] D. Dickertmann, F.D. Koppitz, J.W. Schultze, Eine methode zum ausschluss von randeffekten bei elektrochemischen messungen an einkristallen., Electrochim. Acta. 21 (1976) 967–971. doi:10.1016/0013-4686(76)85072-4.

[40] A.H. Reksten, H. Thuv, F. Seland, S. Sunde, The oxygen evolution reaction mechanism at IrxRu1−xO2powders produced by hydrolysis synthesis, J. Electroanal. Chem. 819 (2018) 547–561. doi:10.1016/j.jelechem.2018.04.018.

[41] W.H. Press, S.A. Teukolsky, W.T. Vetterling, B.P. Flannery, Numerical recipes, Cambridge, 1994.

[42] T. Pajkossy, L.A. Kibler, D.M. Kolb, Voltammetry and impedance measurements of Ir(111) electrodes in aqueous solutions, J. Electroanal. Chem. (2005). doi:10.1016/j.jelechem.2005.03.019.

[43] S. Cherevko, S. Geiger, O. Kasian, A. Mingers, K.J.J. Mayrhofer, Oxygen evolution activity and stability of iridium in acidic media. Part 2. - Electrochemically grown hydrous iridium oxide, J. Electroanal. Chem. (2016). doi:10.1016/j.jelechem.2016.05.015.

[44] S. Cherevko, S. Geiger, O. Kasian, A. Mingers, K.J.J. Mayrhofer, Oxygen evolution activity and stability of iridium in acidic media. Part 1. - Metallic iridium, J. Electroanal. Chem. 773 (2016) 69–78. doi:10.1016/j.jelechem.2016.04.033.

[45] S. Motoo, N. Furuya, Hydrogen and oxygen adsorption on Ir (111), (100) and (110) planes, J. Electroanal. Chem. (1984). doi:10.1016/0368-1874(84)87078-1.

[46] S. Motoo, N. Furuya, Effect of anions on hydrogen and oxygen adsorption on iridium single cyrstal surfaces, J. Electroanal. Chem. (1984). doi:10.1016/0368-1874(84)83638-2.

[47] L.-J. Wan, M. Hara, J. Inukai, K. Itaya, In situ scanning tunneling microscopy of well-defined Ir(111) surface: high-resolution imaging of adsorbed sulfate, J. Phys. Chem. B. (1999). doi:10.1021/jp991112j.

[48] J.-P. Diard, B. Le Gorrec, C. Montella ', C. Montero-Ocampo, Calculation, simulation and interpretation of electrochemical impedance diagrams Part IV. Second-order electrochemical impedances, J. Electroanal. Chem. Elsevier Sequoia S.A. 352 (1993) 1–15.

[49] E. Sibert, R. Faure, R. Durand, High frequency impedance measurements on Pt(111) in sulphuric and perchlorique acids, J. Electroanal. Chem. 515 (2001) 71–81.

[50] M.H. Martin, A. Lasia, Influence of experimental factors on the constant phase element behavior of Pt electrodes, in: Electrochim. Acta, 2011: pp. 8058–8068. doi:10.1016/j.electacta.2011.02.068.

[51] V.M.-W. Huang, V. Vivier, I. Frateur, M.E. Orazem, B. Tribollet, The global and local impedance response of a blocking disk electrode with local constant-phase-element behavior, J. Electrochem. Soc. (2007). doi:10.1149/1.2398889.

[52] G.J. Brug, A.L.G. van den Eeden, M. Sluyters-Rehbach, J.H. Sluyters, The analysis of electrode impedances complicated by the presence of a constant phase element, J. Electroanal. Chem. 176 (1984) 275–295. doi:10.1016/S0022-0728(84)80324-1.

[53] S. Gottesfeld, S. Srinivasan, Electrochemical and optical studies of thick oxide layers on iridium and their electrocatalytic activities for the oxygen evolution reaction, J. Electroanal. Chem. 86 (1978) 89–104.

[54] J. Augustynski, M. Koudelka, J. Sanchez, B.E. Conway, ESCA study of the state of iridium and oxygen in electrochemically and thermally formed iridium oxide films, J. Electroanal. Chem. (1984). doi:10.1016/S0022-0728(84)80128-X.

[55] H.Y. Hall, P.M.A. Sherwood, X-ray photoelectron spectroscopic studies of the iridium electrode system, J. Chem. Soc. Faraday Trans. 1 Phys. Chem. Condens. Phases. 80 (1984) 135–152. doi:10.1039/F19848000135.

[56] J. Mozota, B.E. Conway, Surface and bulk processes at oxidized iridium electrodes-I. Monolayer stage and transition to reversible multilayer oxide film behaviour, Electrochim. Acta. (1983). doi:10.1016/0013-4686(83)85079-8.

[57] E.J. Frazer, R. Woods, The oxygen evolution reaction on cycled iridium electrodes, J. Electroanal. Chem. 102 (1979) 127–130. doi:10.1016/S0022-0728(79)80036-4.

[58] B.E. Conway, J. Mozota, Surface and bulk processes at oxidized iridium electrodes-II. Conductivity-switched behaviour of thick oxide films, Electrochim. Acta. (1983). doi:10.1016/0013-4686(83)85080-4.

[59] E. Özer, C. Spöri, T. Reier, P. Strasser, Iridium(111), Iridium(110), and Ruthenium(0001) single crystals as model catalysts for the oxygen evolution reaction: insights into the electrochemical oxide formation and electrocatalytic activity, ChemCatChem. 8 (2017) 1–8. doi:10.1002/cctc.201600423.

[60] S.J. Freakley, J. Ruiz-Esquius, D.J. Morgan, The X-ray photoelectron spectra of Ir, IrO2 and IrCl3 revisited, Surf. Interface Anal. 49 (2017) 794–799. doi:10.1002/sia.6225.

[61] V. Pfeifer, T.E. Jones, J.J. Velasco Vélez, C. Massué, M.T. Greiner, R. Arrigo, D. Teschner, F. Girgsdies, M. Scherzer, J. Allan, M. Hashagen, G. Weinberg, S. Piccinin, M. Hävecker, A. Knop-Gericke, R. Schlögl, The electronic structure of iridium oxide electrodes active in water splitting, Phys. Chem. Chem. Phys. 18 (2016) 2292–2296. doi:10.1039/c5cp06997a.

[62] V.A. Saveleva, L. Wang, D. Teschner, T. Jones, A.S. Gago, K. Andreas Friedrich, S. Zafeiratos, R. Schlo, E.R. Savinova, Operando evidence for a universal oxygen evolution mechanism on thermal and electrochemical iridium oxides, J. Phys. Chem. Lett. 9 (2018). doi:10.1021/acs.jpclett.8b00810.

[63] M. Peuckert, XPS study on thermally and electrochemically prepared oxidic adlayers on iridium, Surf. Sci. 144 (1984) 451–464. doi:10.1016/0039-6028(84)90111-0.

[64] V.I. Birss, C. Bock, H. Elzanowska, Hydrous Ir oxide films: the mechanism of the anodic prepeak reaction, Can. J. Chem. 75 (1997) 1687–1693.

[65] D.. Whelan, L.D. Burke, A voltammetric investigation of the charge storage reactions of hydrous iridium oxide layers, J. Electroanal. Chem. 162 (1984) 121–141.

[66] S. Geiger, O. Kasian, B.R. Shrestha, A.M. Mingers, K.J.J. Mayrhofer, S. Cherevko, Activity and stability of electrochemically and thermally treated iridium for the oxygen evolution reaction, J. Electrochem. Soc. 163 (2016) F3132–F3138. doi:10.1149/2.0181611jes.

[67] O. Kasian, J.P. Grote, S. Geiger, S. Cherevko, K.J.J. Mayrhofer, The common intermediates of oxygen ovolution and dissolution reactions during water electrolysis on iridium, Angew. Chemie - Int. Ed. 57 (2018) 2488–2491. doi:10.1002/anie.201709652.

[68] V. Pfeifer, T.E. Jones, J.J. Velasco Vélez, R. Arrigo, S. Piccinin, M. Hävecker, A. Knop-

Gericke, R. Schlögl, In situ observation of reactive oxygen species forming on oxygen-evolving iridium surfaces, Chem. Sci. (2017). doi:10.1039/C6SC04622C.

[69] K.B. Oldham, N.P.C. Stevens, Uncompensated resistance. 2. The effect of reference electrode nonideality, Anal. Chem. 72 (2000) 3981–3988. doi:10.1021/ac000154x.

[70] V. Pfeifer, T.E. Jones, S. Wrabetz, C. Massué, J.J. Velasco Vélez, R. Arrigo, M. Scherzer, S. Piccinin, M. Hävecker, A. Knop-Gericke, R. Schlögl, Reactive oxygen species in iridium-based OER catalysts, Chem. Sci. (2016). doi:10.1039/C6SC01860B.

[71] Y.T. Kim, P.P. Lopes, S.A. Park, A.Y. Lee, J. Lim, H. Lee, S. Back, Y. Jung, N. Danilovic, V. Stamenkovic, J. Erlebacher, J. Snyder, N.M. Markovic, Balancing activity, stability and conductivity of nanoporous core-shell iridium/iridium oxide oxygen evolution catalysts, Nat. Commun. 8 (2017) 1–8. doi:10.1038/s41467-017-01734-7.

[72] J.-P. Diard, B. Le Gorrec, C. Montella, Cinétique Electrochimique, Hermann, 1996.

[73] T. Li, O. Kasian, S. Cherevko, S. Zhang, S. Geiger, C. Scheu, P. Felfer, D. Raabe, B. Gault, K.J.J. Mayrhofer, Atomic-scale insights into surface species of electrocatalysts in three dimensions, Nat. Catal. 1 (2018) 300–305. doi:10.1038/s41929-018-0043-3.

[74] O. Kasian, S. Geiger, K.J.J. Mayrhofer, S. Cherevko, Electrochemical on-line ICP-MS in electrocatalysis research, Chem. Rec. (2018) 1–14. doi:10.1002/tcr.201800162.

[75] P. Jovanovič, N. Hodnik, F. Ruiz-Zepeda, I. Arčon, B. Jozinović, M. Zorko, M. Bele, M. Šala, V.S. Šelih, S. Hočevar, M. Gaberšček, Electrochemical dissolution of iridium and iridium oxide particles in acidic media: transmission electron microscopy, electrochemical flow cell coupled to inductively coupled plasma mass spectrometry, and X-ray absorption spectroscopy study, J. Am. Chem. Soc. 139 (2017) 12837–12846. doi:10.1021/jacs.7b08071.

[76] S. Geiger, O. Kasian, M. Ledendecker, E. Pizzutilo, A.M. Mingers, W.T. Fu, O. Diaz-Morales, Z. Li, T. Oellers, L. Fruchter, A. Ludwig, K.J.J. Mayrhofer, M.T.M. Koper, S. Cherevko, The stability number as a metric for electrocatalyst stability benchmarking, Nat. Catal. 1 (2018) 508–515. doi:10.1038/s41929-018-0085-6.

[77] J.P. Meyers, M. Doyle, R.M. Darling, J. Newman, The impedance response of a porous electrode composed of intercalation particles, J. Electrochem. Soc. 147 (2000) 2930. doi:10.1149/1.1393627.

[78] L.A.P. Da Silva, V.A. Alves, M.A.P. Da Silva, S. Trasatti, J.F.C. Boodts, Oxygen evolution in acid solution on IrO2 + TiO2 ceramic films. A study by impedance, voltammetry and SEM, Electrochim. Acta. 42 (1997) 271–281. doi:10.1016/0013-4686(96)00160-0.

[79] J.O.M. Bockris, Kinetics of activation controlled consecutive electrochemical reactions: Anodic evolution of oxygen, J. Chem. Phys. (1956). doi:10.1063/1.1742616.

[80] A.I. Krasilshchikov, Intermediate stages of oxygen anodic evolution, Zhurnal Fiz. Khimii. 37 (1963) 531–537.

[81] E. Fabbri, A. Habereder, K. Waltar, R. Kötz, T.J. Schmidt, Developments and perspectives of oxide-based catalysts for the oxygen evolution reaction, Catal. Sci. Technol. 4 (2014) 3800–3821. doi:10.1039/c4cy00669k.

[82] E. Rasten, G. Hagen, R. Tunold, Electrocatalysis in water electrolysis with solid polymer electrolyte, in: Electrochim. Acta, 2003. doi:10.1016/j.electacta.2003.04.001.

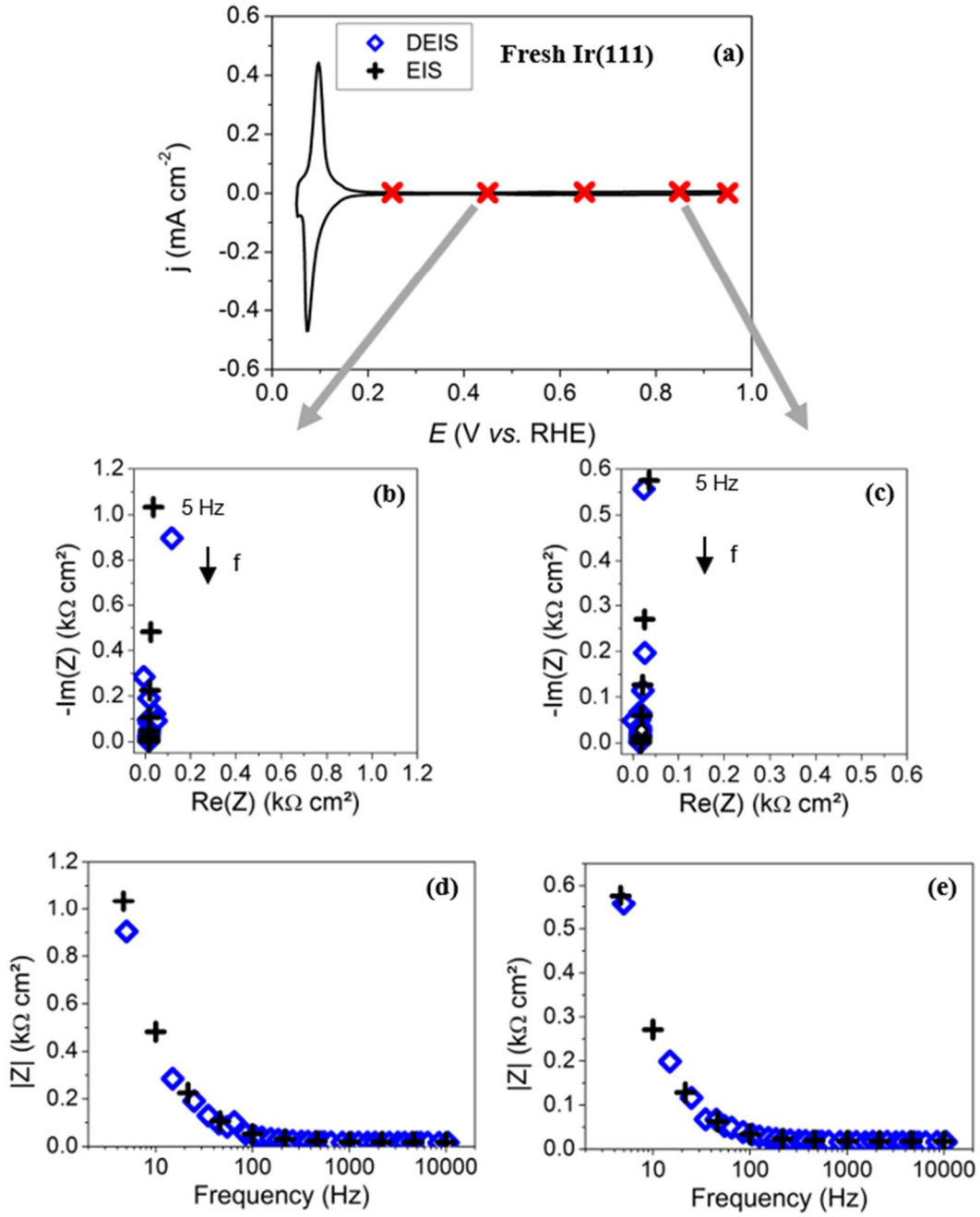

Figure 1. (a) Cyclic voltammogram of as-prepared Ir(111) electrode in 0.05 M H_2SO_4 (potential sweep rate = 50 mV s^{-1}). Red crosses display the potential at which EIS measurements were performed. (b and c) Nyquist plots recorded at 0.45 V and 0.85 V *vs*. RHE, respectively. (d and e) Bode plots recorded at 0.45 V and 0.85 V *vs*. RHE, respectively. Frequency range 10 kHz - 5 Hz. (◊) and (+) symbols represent DEIS and EIS traces, respectively. Note that a fresh Ir(111) electrode was used for each EIS measurement.

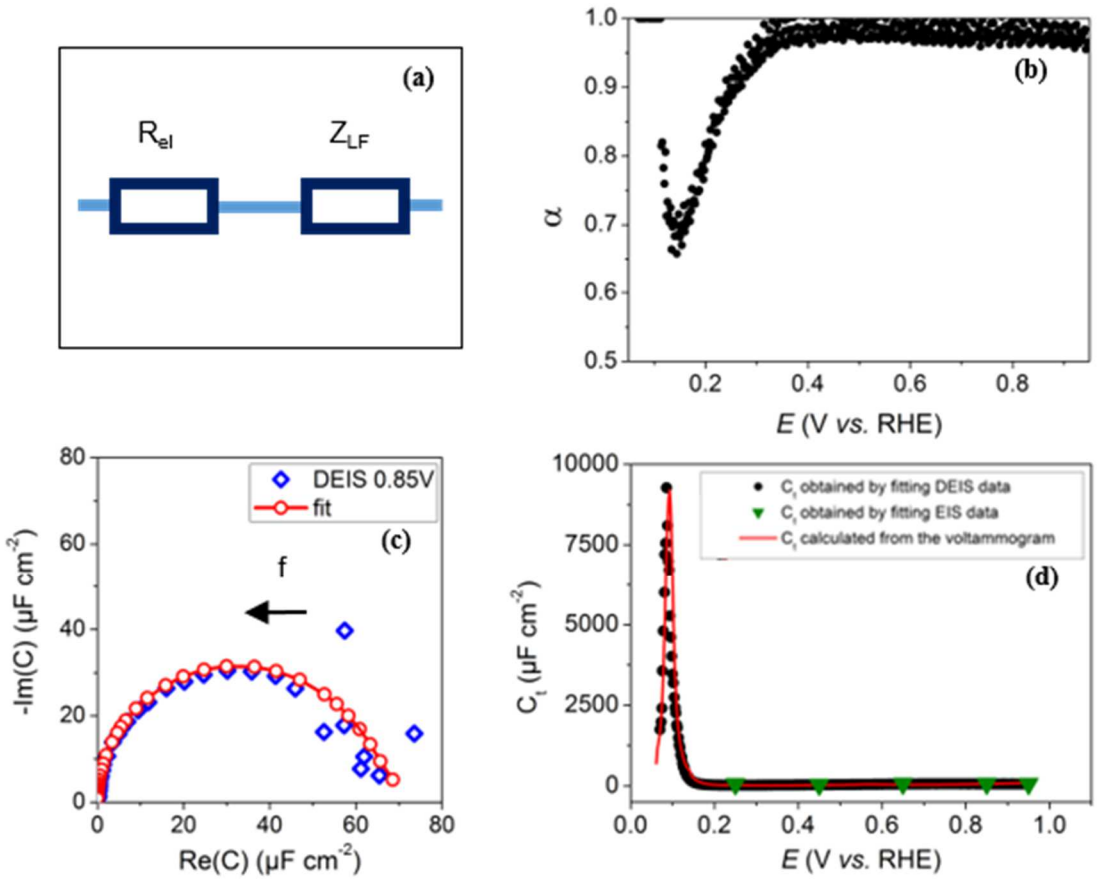

Figure 2. (a) Schematic representation of the equivalent circuit used to fit the impedance data on as-prepared Ir(111). (b) Constant-phase element exponent as a function of the electrode potential. (c) Complex capacitance representation at 0.85 V *vs*. RHE (d) Capacitances calculated from the CVs with Eq. 7 from the fit of EIS and DEIS data with Eq. 6, as a fonction of the electrode potential

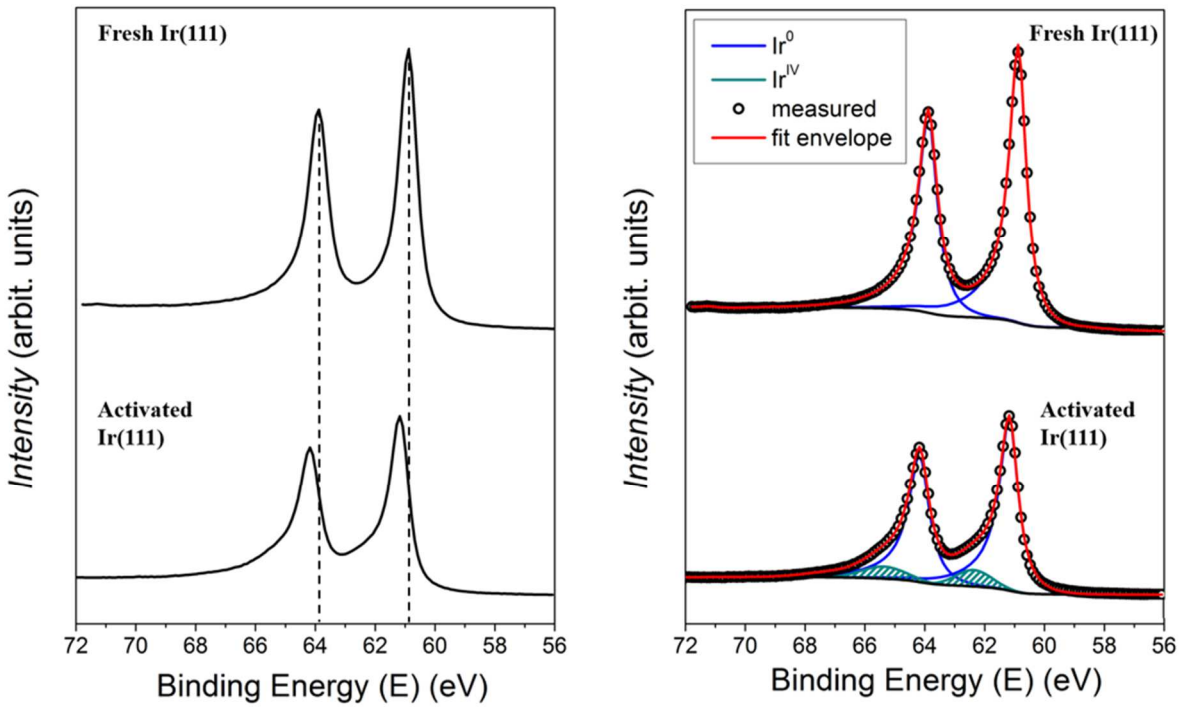

Figure 3. X-ray photoelectron spectra (Ir4f level) of fresh Ir(111) and electrochemically-activated Ir(111).

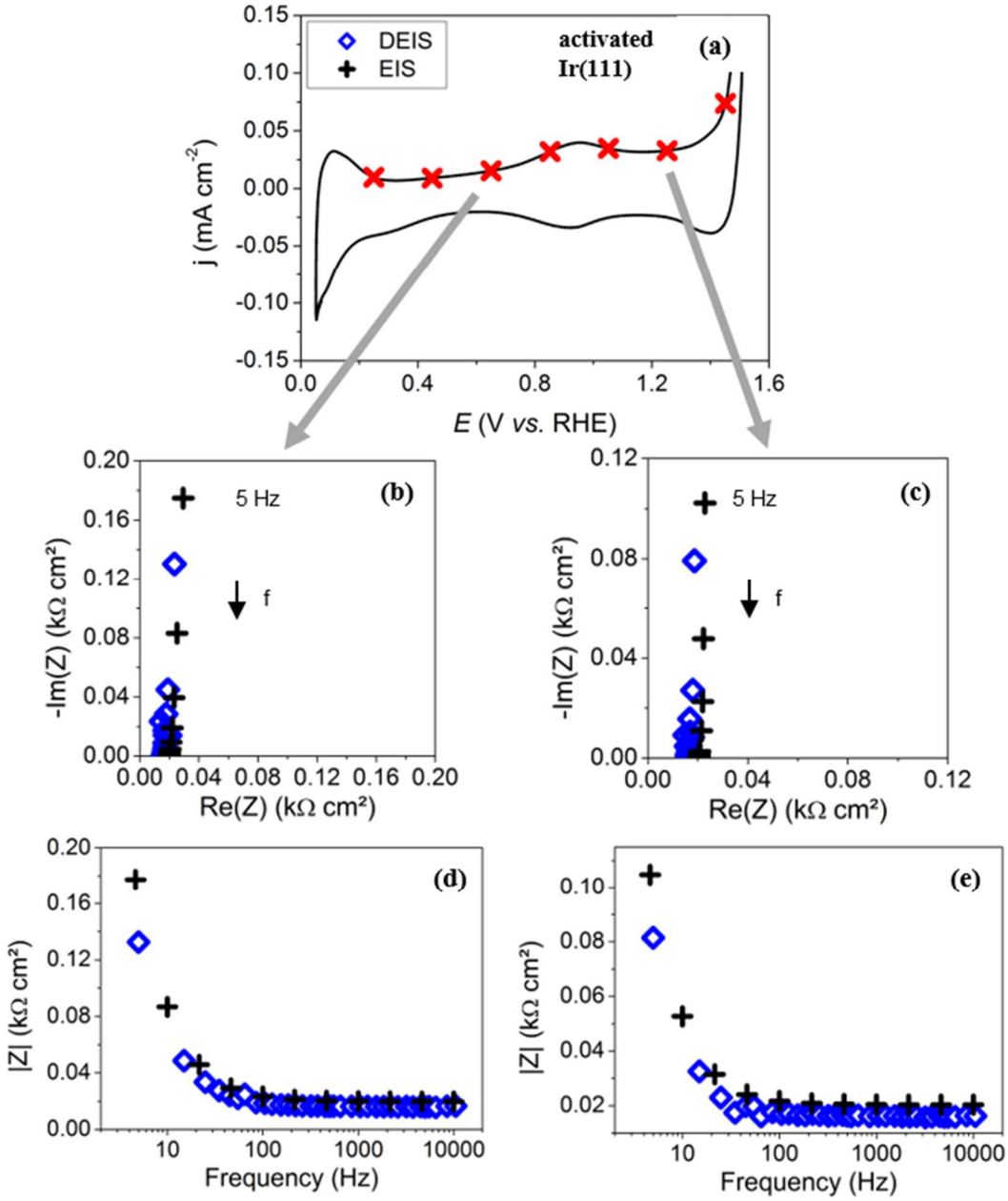

Figure 4. (a) Cyclic voltammogram of 'electrochemically-activated' Ir(111) in 0.05 M H_2SO_4 (potential sweep rate = 50 mV s^{-1}). Red crosses indicate the potential at which EIS measurements were performed. (b and c) Nyquist plots recorded at 0.65 V and 1.25 V *vs*. RHE, respectively. (d and e) Bode plots recorded at 0.65 V and 1.25 V *vs*. RHE, respectively. Frequency range 10 kHz - 5 Hz. (◊) and (+) symbols represent DEIS and EIS data, respectively. Note that an 'electrochemicaly-activated' Ir(111) electrode was used for each EIS measurement.

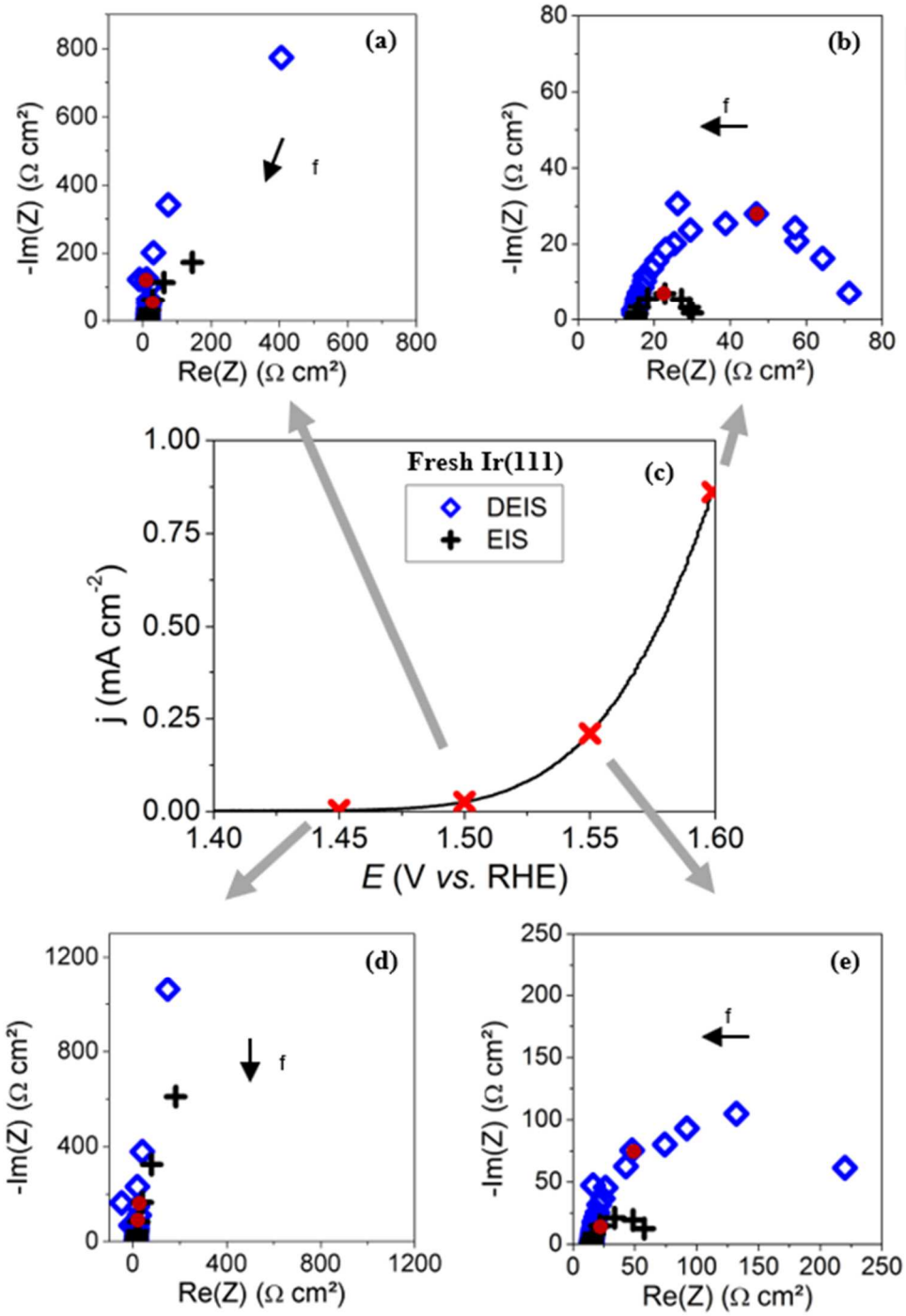

Figure 5. (c) Linear sweep voltammogram of as-prepared Ir(111) in 0.05 M H_2SO_4 (potential sweep rate = 5 mV s^{-1}). Red crosses display the potential at which EIS measurements were performed. (d and a) Nyquist plots measured at 1.45 V and 1.50 V *vs.* RHE, respectively. (e and b) Nyquist plots measured at 1.55 V and 1.60 V *vs*. RHE, respectively. Frequency range 10 kHz – 2.5 Hz. (◊) and (+) symbols represent DEIS and EIS data, respectively. Red dots indicate 45 Hz.

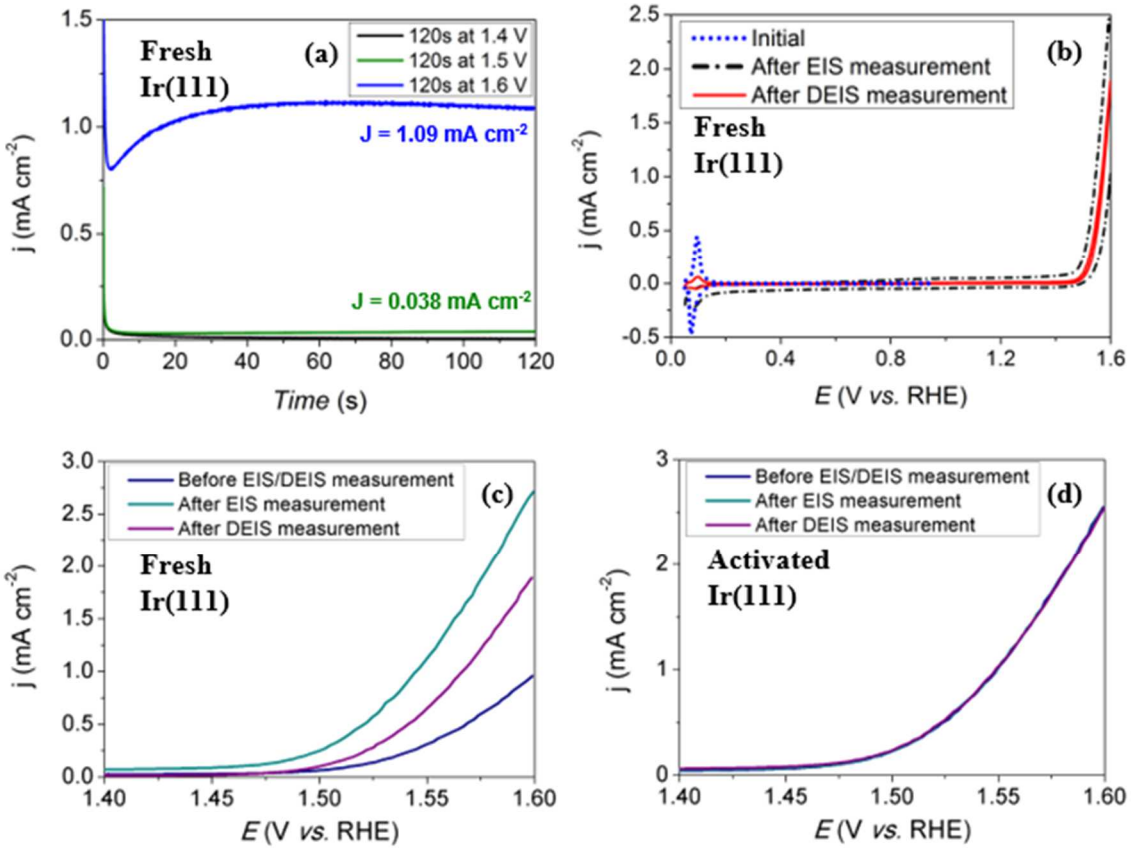

Figure 6. (a) Chronoamperometry recorded on as-prepared Ir(111) recorded at different electrode potentials. Each potential was held for 2 min. (b) Cyclic voltammograms of as-prepared Ir(111) electrode after EIS and DEIS measurements, respectively (potential sweep rate = 50 mV s^{-1}, 0.05 M H_2SO_4) (c) Linear sweep voltammograms of as-prepared Ir(111) electrode before and after EIS and DEIS measurements (potential sweep rate = 50 mV s^{-1}, 0.05 M H_2SO_4) (d) Linear sweep voltammograms of electrochemically-activated Ir(111) before and after EIS and DEIS measurements (potential sweep rate = 50 mV s^{-1}, 0.05 M H_2SO_4) Note that the current density is reported to the geometric surface area and not to the active surface area which changes over time.

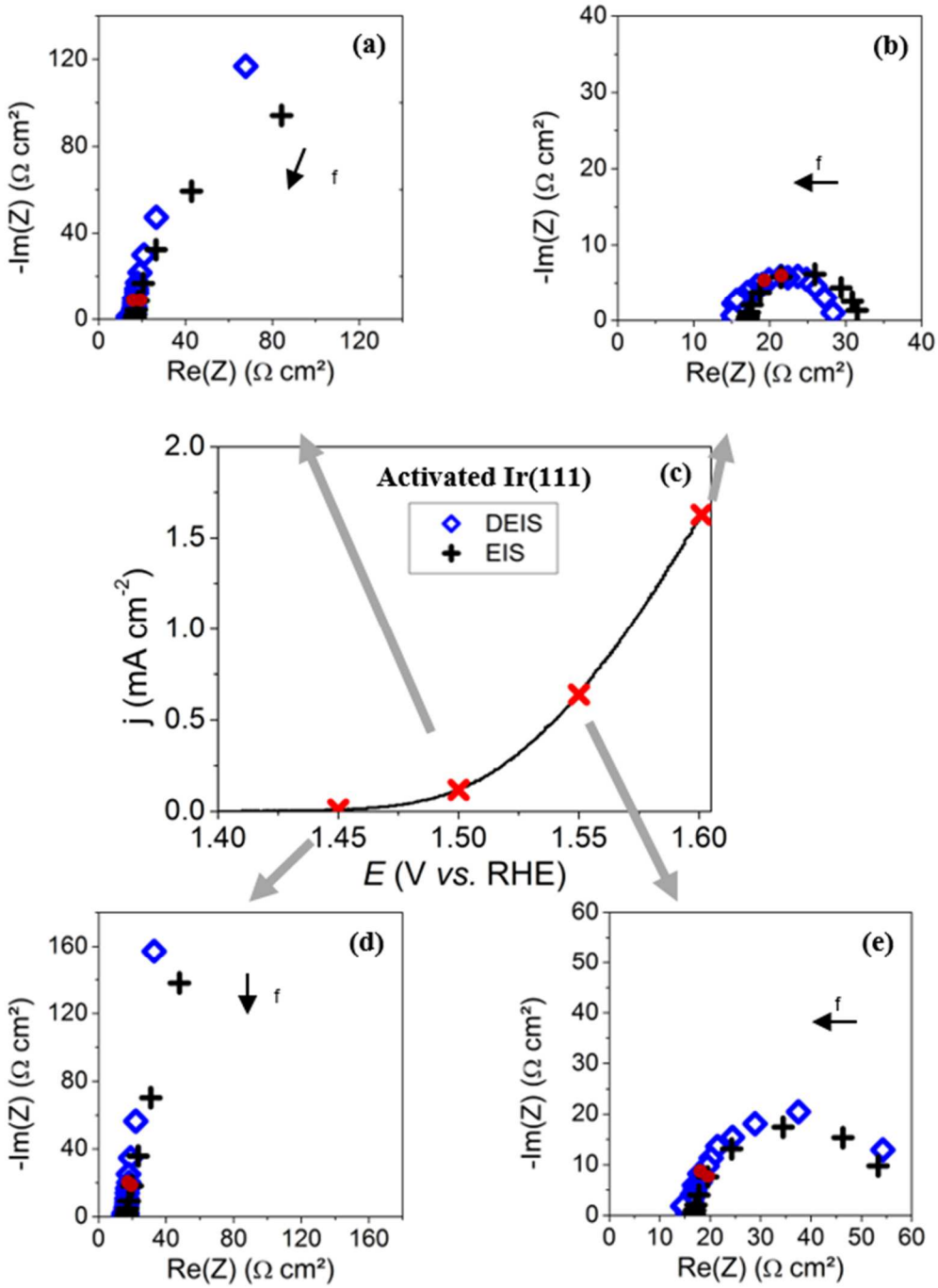

Figure 7. (c) Linear sweep voltammogram of electrochemically-activated Ir(111) in 0.05M H_2SO_4 at 5 mV s^{-1}. Red crosses display the potential at which EIS measurements were performed. (d,a,e,c) Nyquist plots recorded at 1.45 V, 1.50, 1.55 and 1.60 V *vs*. RHE, respectively. Frequency range 10 kHz – 2.5 Hz. (◊) and (+) symbols represent DEIS and EIS traces, respectively. Red dots indicates 45 Hz.

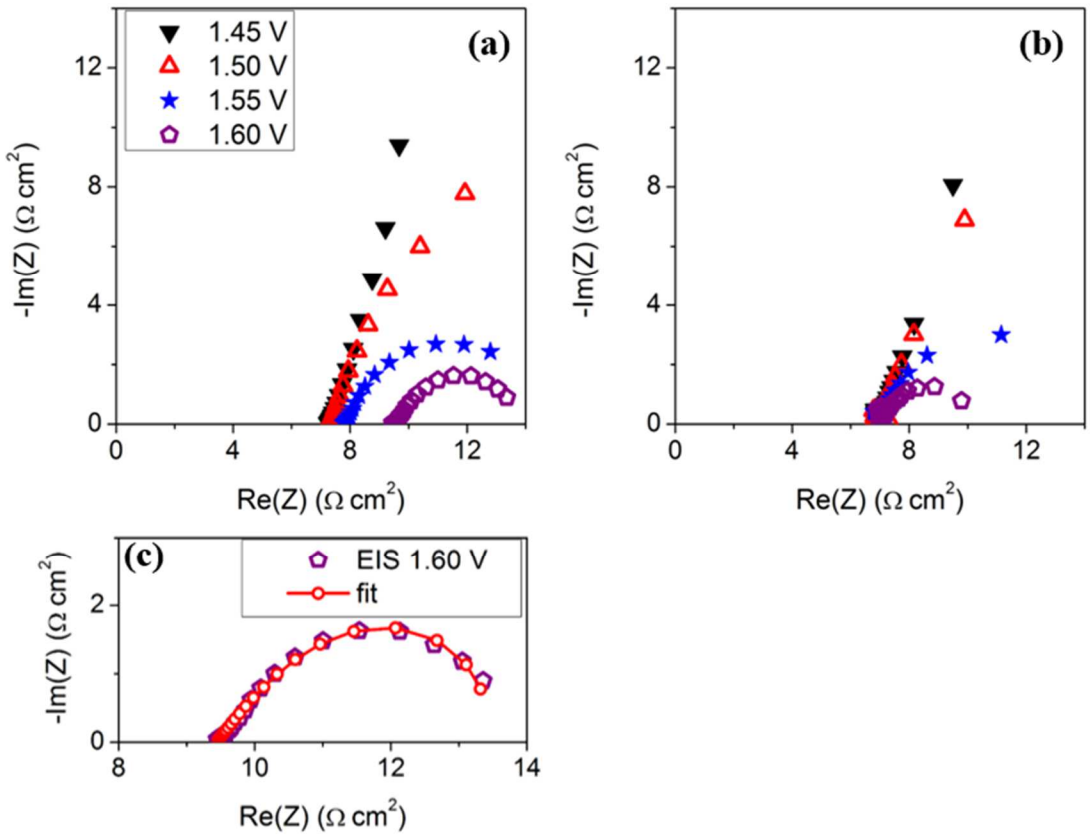

Figure 8. Nyquist plots recorded on Ir nanoparticles supported on Vulcan XC72 at different electrode potentials with (a) EIS and (b) DEIS. Frequency range 10 kHz – 2.5 Hz. (c) Nyquist plot at 1.60 V *vs*. RHE.

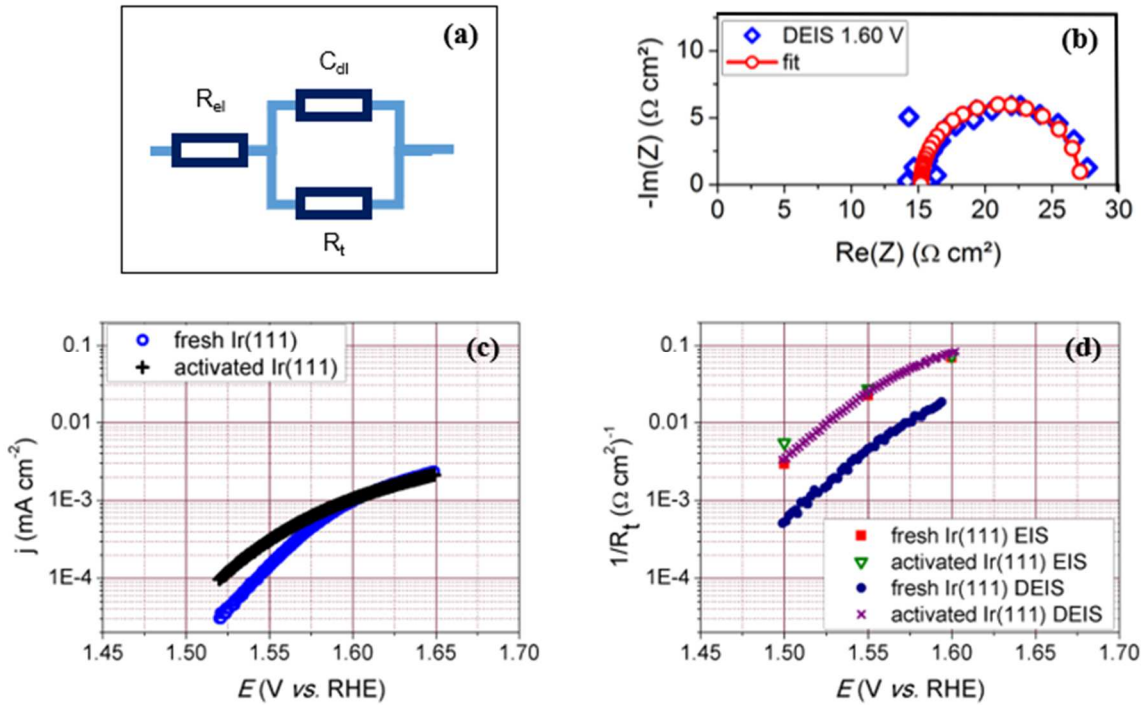

Figure 9. (a) Schematic representation of the equivalent circuit used to fit the data. (b) Nyquist plot at 1.60 V *vs*. RHE. (c) Polarisation curves of as-prepared Ir(111) and electrochemically-activated Ir(111) at 1 mV s^{-1}. (d) Reciprocal of charge transfer resistance obtained by fitting the EIS and DEIS graphs *vs* potential.

Table 1. Ir concentrations measured by ICP-MS in electrolytes after EIS and DEIS measurements on as-prepared Ir(111) and 'electrochemically-activated' Ir(111) electrodes.

	As-prepared Ir(111)	**Electrochemically-activated Ir(111)**
EIS	0.198 ± 7.10^{-3} µg L^{-1}	0.361 ± 0.02 µg L^{-1}
DEIS	0.076 ± 3.10^{-3} µg L^{-1}	0.278 ± 0.01 µg L^{-1}

Table 2. Tafel slopes obtained from the polarization curve at low current densities and calculated from the charge transfer resistance obtained from the EIS/DEIS fits.

Tafel coefficients	**Polarization curves (low current densities)**	**EIS**	**DEIS**
As-prepared Ir(111)	46 mV dec^{-1}	75 mV dec^{-1}	60 mV dec^{-1}
Electrochemically-activated Ir(111)	46 mV dec^{-1}	85 mV dec^{-1}	56 mV dec^{-1}
Theoretical value Electrochemical oxide path (rds: 2nd electrochemical step/chemical step)	40 mV dec^{-1}/24 mV dec^{-1}		
Theoretical value Oxide path (rds: chemical steps)	60 mV dec^{-1}		